Journal of Alloys and Metallurgical Systems 12 (2025) 100219

Contents lists available at ScienceDirect

Journal of Alloys and Metallurgical Systems

journal homepage: www.journals.elsevier.com/journal-of-alloys-and-metallurgical-systems

Design of lightweight high-temperature structural materials based on Ti-Mo-Ta-Cr-Al refractory compositionally complex alloys, Part I: Phase stability and mechanical properties

Amin Radi [a], Daniel Schliephake [a], Sandipan Sen [a], R.J. Vikram [a], Shubhashis Dixit [a], Jan Lars Riedel [a], Liu Yang [a], Chongchong Tang [a], Bronislava Gorr [a], Alexander Kauffmann [b,*], Martin Heilmaier [a]

[a] Institute for Applied Materials (IAM), Karlsruhe Institute of Technology (KIT), Engelbert-Arnold-Str. 4, Karlsruhe 76131, Germany
[b] Institute for Materials (IM), Ruhr University Bochum (RUB), Universitätsstr. 150, Bochum 44780, Germany

ARTICLE INFO

Keywords:
Refractory compositionally complex alloy (RCCA)
Mechanical properties
High temperature
Disordered A2
Single phase
Ti-alloys

ABSTRACT

This study presents the design and evaluation of Ti-rich refractory complex concentrated alloys (RCCAs) within the Ta-Mo-Ti-Cr-Al system, aiming for low density and high-temperature stability. Alloys containing 44–54 at% Ti were synthesized and assessed for phase stability, microstructural evolution, and mechanical performance up to 1000 °C. All compositions primarily exhibit a single-phase disordered A2 structure, even after prolonged thermal exposure. A minor C15 Laves phase appears in Cr- and Ta-rich compositions, with Mo content playing a critical role in its formation. The alloys show significant plasticity at room temperature and maintain high strength at elevated temperatures. Among them, the 44Ti-20Mo-15Ta-15Cr-6Al (at%) composition offers the best balance of thermal stability and mechanical performance at a density of (7.5 ± 0.1) g/cm^3. Compared to commercial Ti- and Ni-based alloys, the designed RCCAs demonstrate superior strength retention above 570 °C, both in absolute and specific yield strength, outperforming single-phase Ti- and Ni-based alloys up to 1000 °C.

1. Introduction

Ti-based alloys are widely recognized for their low density of (~ 4.5 g/cm^3) and high specific strength making them essential in aerospace, biomedical, and high-performance engineering applications [1]. Their mechanical properties, microstructure and thermal stability can be tailored through alloying, thermomechanical processing, and heat treatment. The primary phases in Ti alloys include the hexagonal close-packed (HCP, A3 crystal structure, space group $P6_3/mmc$, Mg prototype) α phase at lower temperatures and the body-centered cubic (BCC, A2 crystal structure, space group $Im\bar{3}m$, W prototype) β phase at higher temperatures. Additionally, metastable phases such as HCP α′, Orthorhombic α″ (orthorhombic martensite, *Cmcm*), and β′ (BCT, tetragonal, space group Im$\bar{3}$m, distorted version of the β (BCC) phase) can form under specific conditions, contributing to enhanced strength and/or toughness [2–4]. While α and near-α Ti alloys offer superior creep resistance and oxidation stability, their limited ductility and formability restrict their use in complex geometries [5]. In contrast, β and near-β alloys exhibit improved ductility and workability but suffer from reduced oxidation resistance and microstructural instability at elevated temperatures [6–8]. Therefore, multi-phase Ti alloys are typically limited to 600 °C in air, where oxidation and microstructural coarsening begin to degrade performance. [9,10]. Multi-phase titanium aluminides (e.g., Ti-48Al-2Cr-2Nb with γ/α_2 microstructure), where γ-TiAl is a tetragonal and α_2-Ti_3Al an ordered hexagonal phase, have been developed to extend this range to about 700 °C, also offering low density and high specific strength [11]. With the application of advanced oxidation-resistant coatings, γ-TiAl-based alloys have demonstrated potential for use at temperatures up to 750 °C and beyond [12]. However, their intrinsic brittleness at room temperature (RT) remains a major barrier to their widespread application [13].

Ni-based superalloys are the current standard for structural applications up to 1100 °C, due to their strength, creep resistance, and oxidation stability [14,15]. These alloys are typically composed of a face-centered cubic (FCC) γ matrix phase (A1 crystal structure, Fm$\bar{3}$m space group, Cu prototype), where the γ phase refer to the primary solid

* Corresponding author.
E-mail address: alexander.kauffmann@rub.de (A. Kauffmann).

https://doi.org/10.1016/j.jalmes.2025.100219
Received 20 August 2025; Received in revised form 5 October 2025; Accepted 19 October 2025
Available online 21 October 2025

solution matrix. Moreover, the presence of coherent γ′-Ni_3(Al,Ti) precipitates ($L1_2$ crystal structure, $Pm\bar{3}m$ space group, Cu_3Au prototype) in these alloys provides significant precipitate strengthening [16]. The γ′ phase dissolves at a homologous temperature of ~ 0.85 T_s with T_s being the solidus temperature, corresponding to approximately 1235 °C, thereby enabling sustained performance under high thermal and mechanical loads [17]. However, the relatively high density of Ni-based superalloys—such as Rene 80 (8.2 g/cm³), CMSX-4 (8.7 g/cm³), and Rene N5 (8.6 g/cm³)—poses a challenge for weight-sensitive components [18]. Critical elements like W, Zr, Mo, and Ta enhance high-temperature performance but also affect phase stability and microstructural complexity [19]. Their performance degradation at temperatures higher than 1100 °C due to γ′ coarsening and dissolution motivate the search for alternative materials with comparable performance but lower density and cost [20–22].

This highlights a gap for alloys operating between 700–1000 °C and with densities between 4.5 and 8 g/cm³, where Ti- and Ni-based alloys fall short for modern aerospace and energy needs. This gap has motivated the exploration of novel alloy systems that balance strength in high temperatures, RT plastic deformability, oxidation resistance, microstructural stability, and density.

Among emerging candidates, refractory complex concentrated alloys (RCCAs) — a subset of high-entropy alloys — have attracted attention in the past decade [23,24]. Composed of refractory elements such as Ta, Mo, Nb, Hf, W, and Zr, RCCAs are characterized by their high melting (solidus) temperatures and excellent thermal stability. [25–31]. Depending on composition, these alloys can form disordered BCC (A2), ordered B2, or dual-phase A2 +B2 microstructures [24]. However, their usually high densities (~8–13.6 g/cm³), tendency towards brittleness by the presence of the B2 phase, and often poor oxidation resistance limits their applicability in weight-sensitive and high temperature environments [32,33].

Designing RCCAs for high-temperature applications requires balancing multiple competing properties, including low density, RT plastic deformability, high-temperature strength, and oxidation resistance. This study investigates whether Ti-rich RCCAs within the Ta–Mo–Ti–Cr–Al system, which was studied in our group recently and demonstrated a potentially promising property portfolio [34–39], can provide a low density while maintaining a single-phase microstructure with disordered crystal structure. The alloy design is guided by the following criteria:

- Low density (< 7.8 g/cm³): by a Ti basis (44–54 at%) with Cr (10–15 at%) and Al (5–6 at%) addition.
- Single-phase microstructure with disordered A2 crystal structure: by suppressing B2 ordering (Al ≤ 6 at%) and Laves phase formation (Ta ≤ 15 at%, Cr ≤ 15 at%) [36]. These secondary phases typically degrade ductility and mechanical performance [40].
- High temperature strength (600–1000 °C): enabled through the addition of Ta and Mo.
- Oxidation resistance: employing Cr, Al, and Ta, which can promote the formation of protective oxide scales such as Al_2O_3, Cr_2O_3, and (Cr, Ta,Ti)O_2 [37,41]. The high-temperature oxidation behavior is systematically investigated and evaluated in Part II to assess the alloys' suitability for high-temperature applications.

To address these design goals systematically, we employ thermodynamic calculations to guide the alloy design and predict phase stability across the targeted composition and temperature ranges.

2. Materials and methodology

2.1. Materials and processing

Thermodynamic calculations were performed using FactSage V7.2 with an in-house database [38] and Pandat with the PanRHEA2025 database [42], conducted at a step size of 10, 20, and 40 K. The alloys were fabricated employing repetitive arc melting with an AM/0.5 arc melting device by Edmund Buhler GmbH (Germany) under an Ar4.6 atmosphere.

Bulk elements of Ta, Mo, Ti, Cr, and Al were used with purities of 99.9 %, 99.97 %, 99.99 %, 99.995 %, and 99.99 %, respectively.

Alloys were synthesized via repetitive arc melting using an AM/0.5 arc melting device (Edmund Buhler GmbH, Germany) under an Ar4.6 atmosphere. Each alloy underwent five remelting cycles to ensure chemical homogeneity. Prior to each remelting, a Zr lump was melted to act as an O getter and reduce residual O in the chamber.

After casting, the alloys were homogenized at 1400 °C for 48 h in a HRTH 70–600/18 resistance tube furnace (Carbolite Gero GmbH & Co. KG, Germany), with heating and cooling rates of 100 K/h under continuous Ar4.8 flow. The as-cast condition is referred to as AC, and the homogenized condition as HT.

To assess microstructural stability, homogenized samples were subjected to heat treatments at 800 °C and 1000 °C for durations of 10, 100, and 1000 h. Samples were wrapped in Ta foil, encapsulated in evacuated silica tubes filled with Ar4.8, and quenched by breaking the ampoules in water.

2.2. Materials characterization

Samples were ground using water-cooled SiC paper up to P4000 grit, followed by polishing with 3 μm and 1 μm diamond suspensions. Final polishing was performed using a non-crystallizing oxide suspension (Struers, Denmark) mixed with 20 vol% of 30 %-concentrated H_2O_2.

Microstructural analysis was conducted using a LEO Gemini 1530 SEM (Carl Zeiss AG, Germany) in backscattered electron (SEM-BSE) mode at 20 kV. SEM-EDS analysis was performed using a Zeiss EVO50 SEM (Carl Zeiss AG, Germany) equipped with a silicon drift detector (Thermo Fisher Inc., USA) at 25 keV.

The global chemical composition of T1 (48Ti-25Mo-12Ta-10Cr-5Al at%) in the HT condition was determined using inductively coupled plasma optical emission spectrometry (ICP-OES) with an iCAP 7600 DUO (Thermo Fisher Scientific Inc.). These results and the specimen were used as a standard for energy-dispersive X-ray analysis (SEM-EDS). Impurity concentrations of N and O were measured via carrier gas hot extraction (CGHE) using a TC600 system (LECO Corporation, USA) (see Table 1).

Phase identification and lattice parameter determination were performed using a Bruker D2 Phaser (Germany) with a Cu Kα source (30 kV, 10 mA) and a 1D LynxEye detector. Scans were conducted over 10–145° in 2θ with a step size of 0.02° and an accumulated acquisition time of 384 s per step. The lattice parameter a for the three compositions was calculated by extrapolating the peak position to $\theta = 90°$ using the weighted function $w(\theta) = (\cot^2\theta + \cot\theta\cos\theta)$, following the modified strategy by Nelson-Riley [43].

Experimental densities were determined using the Archimedes principle in ethanol at RT, following standard procedures. Theoretical densities were calculated using the lattice parameters, atomic masses, assuming full density and desired composition. For single-phase alloys (T1 and T2), the A2 phase density was used directly. For T3, which contains a minor fraction of Laves phase, the alloy is treated as effectively single-phase for the purpose of theoretical density estimation.

High-temperature differential scanning calorimetry (DSC) experiments were conducted using a DSC 404 F1 Pegasus system equipped with a platinum furnace from Netzsch-Gerätebau GmbH (Germany). The enthalpy derivative with respect to temperature was determined using a sapphire standard as the reference sample, following the DIN 51007:2019-04 standard [44]. The DSC chamber was evacuated and purged three times with high-purity Ar. During the DSC measurements, a Zr getter was employed to remove residual O in the atmosphere. The sample was placed in a Pt-Rh crucible with Al_2O_3 inlays and covered

Table 1
Chemical and physical properties of the alloys designated with T1–T3: desired (des.) and experimentally (exp.) verified chemical composition $\overline{X}_i$, experimental O and N impurity concentration, theoretical and experimental density ρ as well as experimental lattice parameter a.

Designation		$\overline{X}_i$ / at%					$\overline{X}_i$ / wt.-ppm		ρ/g/cm^3	a/Å
		Ti	Mo	Ta	Cr	Al	O	N		
T1	Des.	48.0	25.0	12.0	10.0	5.0	–	–	7.5	–
	Exp.	47.8	25.1	12.1	9.8	5.2	157 ± 39	< 20	7.1 ± 0.1	3.184 ± 0.001
T2	Des.	44.0	20.0	15.0	15.0	6.0	–	–	7.7	–
	Exp.	44.3	20.1	15.1	14.8	5.8	110 ± 28	< 10	7.5 ± 0.1	3.181 ± 0.003
T3	Des.	54.0	10.0	15.0	15.0	6.0	–	–	7.3	–
	Exp.	54.6	9.9	14.7	14.8	5.9	163 ± 41	< 10	7.2 ± 0.1	3.192 ± 0.004

with a Pt-Rh lid. The experiments were conducted with a heating rate of 10 K/min from RT to 1450 °C.

2.3. Mechanical testing

Compression tests were conducted using a Z100 electromechanical universal testing machine from ZwickRoell GmbH & Co. KG (Germany). Compression test samples were manufactured to a size of (3 × 3 × 5) mm^3 using electrical discharge machining, followed by grinding (grit P4000) to ensure flat, coplanar compression surfaces. The compression tests were performed at an initial strain rate of 10^{-3} s^{-1} over a temperature range from RT to 1000 °C, in a vacuum of 10^{-5} mbar in a furnace supplied by Maytec GmbH (Germany). At least three tests were carried out at each temperature to ensure statistical relevance. The 1 % offset yield strength was used for evaluation, as it provides a more robust and consistent measure in compression testing, where the elastic region can be difficult to define accurately due to machine compliance and sample geometry. True stress and true strain values were derived from engineering stress and strain, assuming volume conservation during plastic deformation.

3. Results and discussion

3.1. Thermodynamic calculations and alloy compositions

Multiple alloy compositions were screened using the thermodynamic databases mentioned in the methodology section, based on the design criteria [45]. Out of these, three are selected based on FactSage, as they were predicted to meet the alloying requirements and maintaining a single-phase condition over a large temperature range. The evolution of the phase fractions for the three alloy compositions of 48Ti-25Mo-12-Ta-10Cr-5Al (abbreviated as T1 in what follows), 44Ti-20Mo-15Ta-15C-r-6Al (T2), and 54Ti-10Mo-15Ta-15Cr-6Al (T3)—as a function of temperature obtained via FactSage is illustrated in Fig. 1a–c.

According to the calculations, solidification initiates with the formation of the A2 phase in all three alloys, which dominates the microstructure below the solidus temperature T_S (see Supplementary information Table S1). Notably, the higher Ti content in T3 results in a significantly lower T_S of about 1760 °C compared to 1900 and 2000 °C for T1 and T2, respectively. The solidus temperatures are comparably consistent among the two databases tested (see Supplementary

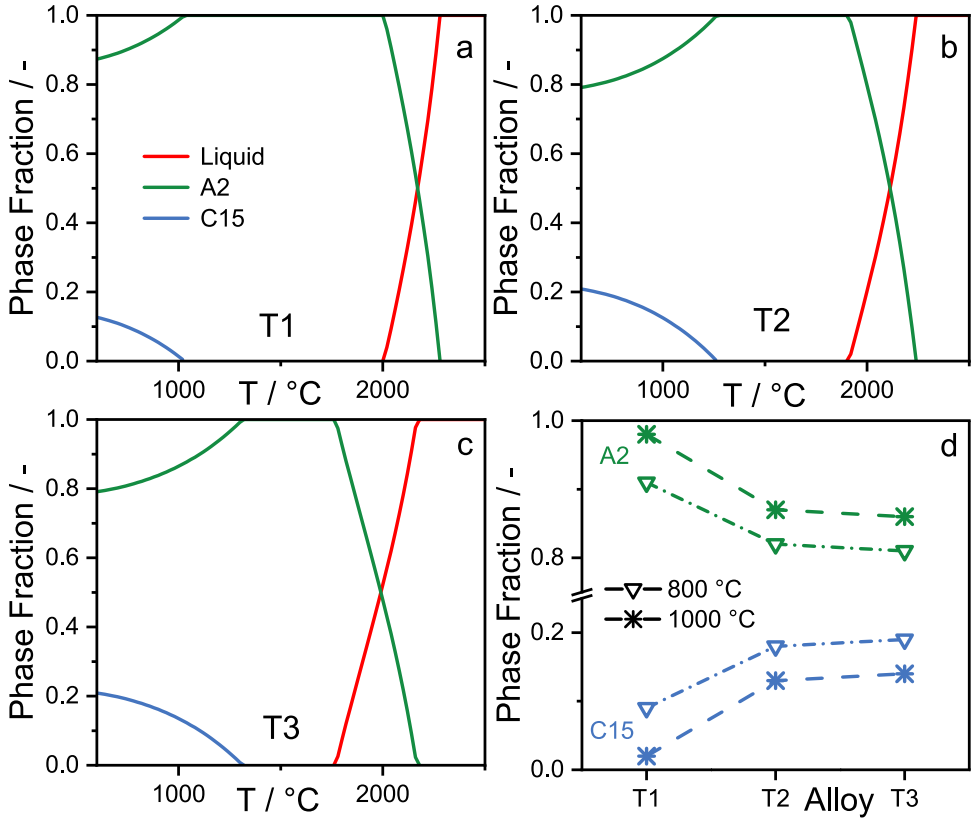

Fig. 1. Thermodynamic calculation of phase fractions as a function of temperature: a) T1, b) T2, c) T3, and d) Phase fractions at 800 and 1000 °C for the three alloys; the connecting lines are to guide the eyes.

information Fig. S1 and Table S1 for the Pandat results).

At lower temperatures of 1000–1300 °C (Fig. 1), thermodynamic calculations via FactSage predict the formation of the C15 Laves phase in considerable amounts, which aligns with prior studies on the Ti-Mo-Ta-Cr-Al system, incl. subsystems [46,47]. Pandat also predicts C15 formation, but at significantly lower temperatures (740–970 °C). Hence, experimental confirmation of the presence of C15 is required. As the nucleation and growth of C15 may be kinetically retarded [48], long-term annealing studies at elevated temperatures are essential. For this study, 800 and 1000 °C were selected, as they cover the intended application range and beyond. Fig. 1d summarizes the equilibrium phase fractions at these temperatures. T1 exhibits the lowest predicted C15 phase fraction, while T3 shows the highest.

B2 may form in the Ta–Mo–Ti–Cr–Al system in two ways: (i) complete ordering of A2 to during cooling via a 2nd order phase transition [34,36] or (ii) B2 precipitation via a nucleation and growth mechanism [35,36,49]. However, the thermodynamic descriptions in these studies were reported to be imprecise [34,36,38], substantially underestimating transformation temperatures and failing to accurately predict the nature of the phase transformations. For the present alloys, B2 is predicted for temperatures lower than 600 °C by the FactSage database. In contrast, Pandat suggests a B2 formation between 600 and 700 °C, see Supplementary information Table S1. In any case, B2 is suggested to form via a 1st order nucleation and growth process [50]. Thus, its volume fraction depends on temperature.

The two databases do not agree on the formation temperatures of the secondary phases C15 and B2. Thus, the potential phase separations need to be assessed via DSC [34] and microstructural analysis [35].

Table 1 presents the desired and experimental chemical composition after synthesis of the alloys. The manufactured alloys closely match the designed compositions as confirmed by standard-related SEM-EDS. The O and N contaminations by raw materials and uptake during homogenization are 200 wt.-ppm and 20 wt.-ppm, respectively. The O and N levels are comparably low for the present synthesis and processing route [36]. The experimentally determined densities of the three alloys are also listed in Table 1. The density design criterion is met.

3.2. Microstructural constitution and phase stability

Fig. 2 displays representative SEM-BSE micrographs for all three alloys in the AC (a-c), HT (d-f), long-term heat treated at 800 °C (g-i), and 1000 °C (j-l) conditions. In the AC condition, all alloys exhibit a dendritic microstructure, with heavy elements, e.g. Ta and Mo, predominantly enriched within the dendrites (bright contrast), while light elements, e.g. Ti and Al, are concentrated in the interdendritic regions (darker contrast) [51]. After homogenization in the HT condition, the microstructure consists of equiaxed, coarse grains with a homogeneous distribution of alloying elements. The homogenization treatment results in relatively coarse grains, with average grain sizes of (552 ± 242) μm for T1, (807 ± 157) μm for T2, and (1625 ± 393) μm for T3. While alloys T1 and T2 remain single-phase in the HT condition, a second phase is observed along the grain boundaries in T3, as shown in the insets of Fig. 2d–f. SEM-EDS analysis of the grain boundary phase in T3 (see Supplementary information Table S2) reveals a Cr-rich phase with a Cr-to-Ta ratio of ~ 1.8:1, consistent with the formation of a Cr_2Ta-type Laves phase. As significant Mo substitution for Ta is observed in this phase, a Cr_2(Ta,Mo) intermetallic solid solution phase is suggested to be present [52].

sA low fraction of pores is observed in the grain interiors and at the grain boundaries for all three alloys following the casting process. Additionally, Kirkendall pores appear during the HT treatment [53]. Based on theoretical and experimental densities, the porosity in the HT condition is calculated to (5.0 ± 1.0), (3.0 ± 1.0), and (1.0 ± 1.0) vol% for T1, T2, and T3, respectively.

XRD analysis in Fig. 3 confirms that T1 is single-phase in both the AC and HT conditions, exhibiting only peaks corresponding to the A2 crystal structure. For T2 and T3, the presence of the C15 Laves phase is indicated alongside the A2 matrix, although it was not observed via microstructural investigations in T2. This is possibly due to its low volume fraction (see Fig. 2e) [54]. No superlattice peaks characteristic of B2 ordering were detected in any of the alloys.

The formation of the C15 Laves phase in T2 and T3 can be correlated with Cr solubility in the matrix phase of the alloys. The trend in Cr solubility in the matrix can be effectively mapped by the A2 lattice parameter, as Cr is by far the smallest atom among the constituent elements (lattice parameter of < 2.9 Å for pure Cr, while > 3.15 Å for the other elements, see Supplementary material Fig. S3). T2 exhibits a slightly lower A2 lattice parameter, indicating more dissolved Cr compared to T1, while the parameter increases in T3 due to Cr depletion following C15 formation. Regarding the C15 Laves phase, Pandat with PanRHEA currently fails to capture experimental observations, as the temperature interval for C15 appearance is strongly underestimated (Supplementary information Table S1).

The clear identification of B2 superstructures in RHEAs using diffraction techniques can be hindered by distinct atomic site occupancies, which may reduce the intensity of characteristic superlattice reflections [34]. Alternatively, thermal analysis techniques are more robust for investigating of the heat signatures of order-disorder (B2-A2) transitions [36] or B2 precipitation [39] in the Ta–Mo–Ti–Cr–Al system. Fig. 4 depicts the DSC results for all three alloys in HT condition during heating. The $\frac{dH}{dT}$ remains almost constant over the entire temperature range investigated. Thus, no evidence of ordering (characterized by a λ-shaped anomaly) or precipitation (heating rate-dependent peak) is observed. For comparison, the λ-shaped heat signature corresponding to the 2nd order phase transformation in equimolar TaMoCrTiAl is included in Fig. 4 [36]. B2 precipitation may be kinetically suppressed in the present alloys, with solvus temperatures predicted below 700 °C, as long-range diffusion would be required [35,55].

As stated above, microstructural (SEM-BSE) and crystallographic (XRD) investigations of the HT condition in Fig. 2 and Fig. 3, respectively, reveal the presence of C15 in T2 and T3, while T1 appears truly single-phase. However, these observations are based on furnace-cooled samples, where kinetic suppression of C15 formation is possible [56]. For high-temperature applications — particularly in aerospace and energy systems — thermal stability at 800 and 1000 °C is critical. Therefore, long-term heat treatments were performed at 800 and 1000 °C for up to 1000 h to evaluate the phase stability and test the thermodynamic predictions. These results are also included in Fig. 2 and Fig. 3, respectively. T1 remains single-phase A2 even after 1000 h at 800 and 1000 °C, as shown in Figs. 2g and 2j, and Fig. 3a. In contrast, C15 formation is observed in T2 (Figs. 2h and 2k, and Fig. 3b) and T3 (Figs. 2i and 2l and Fig. 3c). Additional SEM-BSE micrographs after 10 and 100 h of exposure at these temperatures are depicted in Supplementary information Fig. S2 to illustrate the time-dependent microstructural evolution. At 1000 °C, T2 exhibits a minor amount of C15 with a volume fraction of < 1 vol%, while the fraction of C15 appears to be much higher in T3 with a total of (10.4 ± 1.8) vol%. Notably, a substantial portion of the C15 phase in T3 forms rapidly, with (7.4 ± 0.9) vol% already present after just 100 h of exposure at this temperature (see Supplementary information Fig. S2). This indicates fast phase formation kinetics and that near-equilibrium conditions are reached early during the heat treatment. At 800 °C, C15 is located only at grain boundaries in both T2 and T3, with volume fractions below 1 vol%.

Despite identical Ta and Cr concentrations in T2 and T3, the alloys exhibit markedly different C15 fractions after prolonged high-temperature exposure. The formation of Cr_2(Ta,Mo)-based Laves phase consumes considerable amounts of Cr and Ta from the A2 matrix, resulting in a lattice parameter change in T3 after 1000 h of annealing at 1000 °C (Fig. 3d). This change is not observed in the other conditions, where no or only small amounts of Laves phase form. Thus, maintaining a Mo content of $\geq$ 2 at% appears to be key to effectively suppressing the

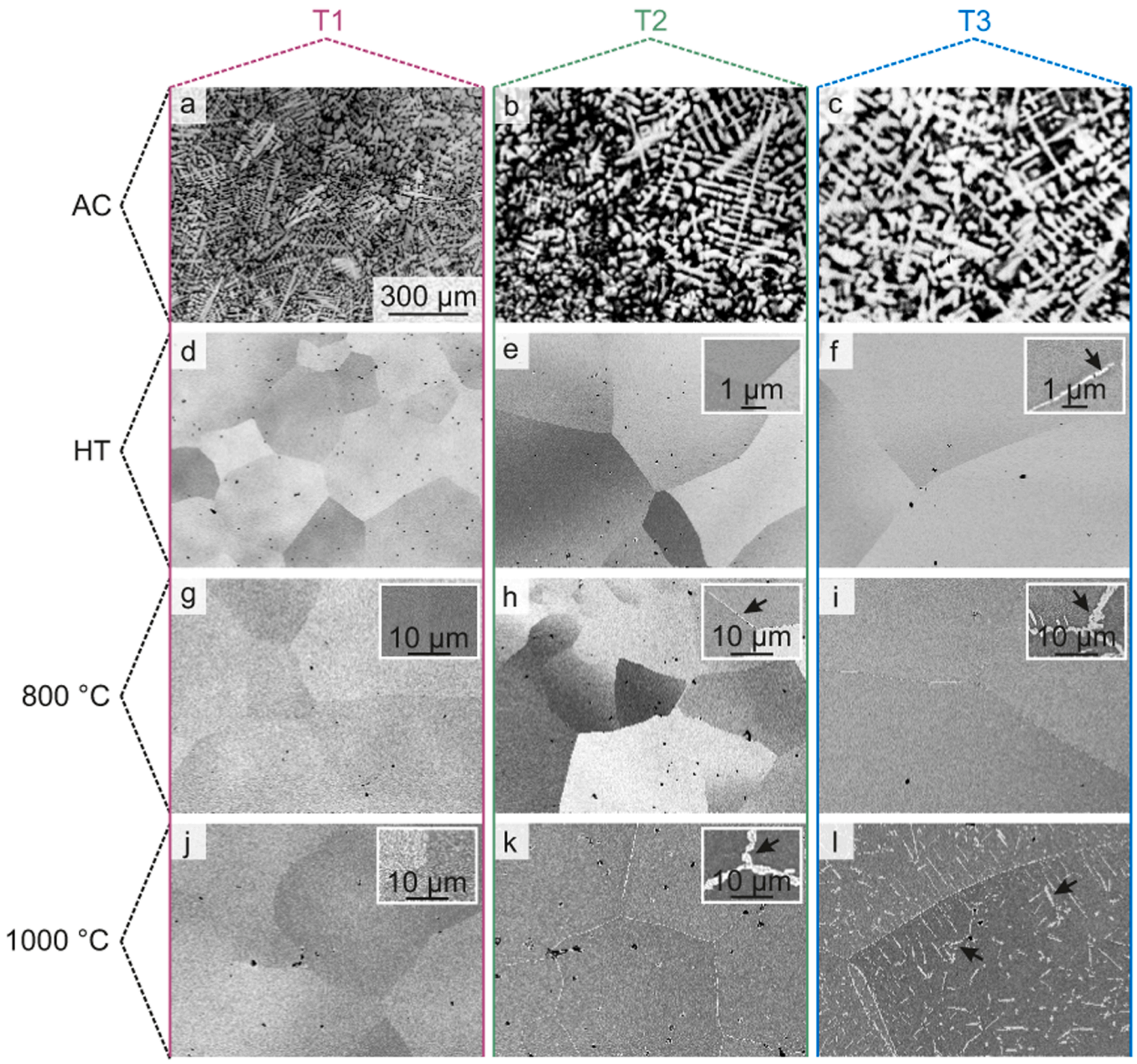

Fig. 2. SEM-BSE micrographs for AC (a–c), HT (d–f), 800 °C/1000 h (g–i) and 1000 °C/1000 h (j–l): a,d,g,j) T1, b,e,h,k) T2, and c,f,i,l) T3. The magnifications are the same for all overview micrographs. The black arrows highlight the C15 phase.

undesired formation of C15.

The C15 phase fractions are overestimated by 2–14 vol%[1] in the thermodynamic calculations (FactSage, Fig. S1), compared to the experimentally obtained 0–10 vol% at 1000 °C (~ 0.63 T_S). According to these thermodynamic calculations, the Laves phase fraction is mainly determined by the Cr/Ta content in the alloys, with an increase of approximately 10 vol% C15 per 5 and 2.5 at% Cr and Ta, respectively (i.e. from T1 to T2/T3). While these predictions capture general trends in phase stability, they fail to account for the influence of Mo on Cr solubility in the A2 matrix, which is critical for suppressing C15 formation. This effect is evident from the A2 lattice parameter evolution, where T2 shows a slightly reduced lattice parameter compared to T1, indicating higher Cr solubility. In contrast, T3 exhibits a significantly increased lattice parameter after 1000 h at 1000 °C, consistent with Cr depletion due to extensive C15 formation. Thus, changes in lattice parameter serve as a sensitive indicator of Cr content in the matrix. Maintaining a Mo content of $\geq$ 20 at% appears essential not only for suppressing C15 formation but also for stabilizing Cr within the A2 phase.

3.3. Mechanical behavior

Fig. 5a–c depicts representative true stress-strain curves from compression tests, calculated using the instantaneous cross-sectional area and logarithmic strain. The 1 % offset yield strength at RT ranges from 1000 to 1250 MPa for all alloys, while T2 exhibits the highest value

[1] Molar mass and densities of A2 and C15 are 70 and 81 g/mol and 7.2 and 9.30 g/cm^3, respectively (Supplementary information Table S3), which gives a density of 7.38 g/cm^3 for T3. Thus, an exact conversion of atomic to volumetric phase fractions leads to changes below the experimental uncertainties and differences between thermodynamic predictions (7.38 g/cm^3) and experiment (7.2 g/cm^3).

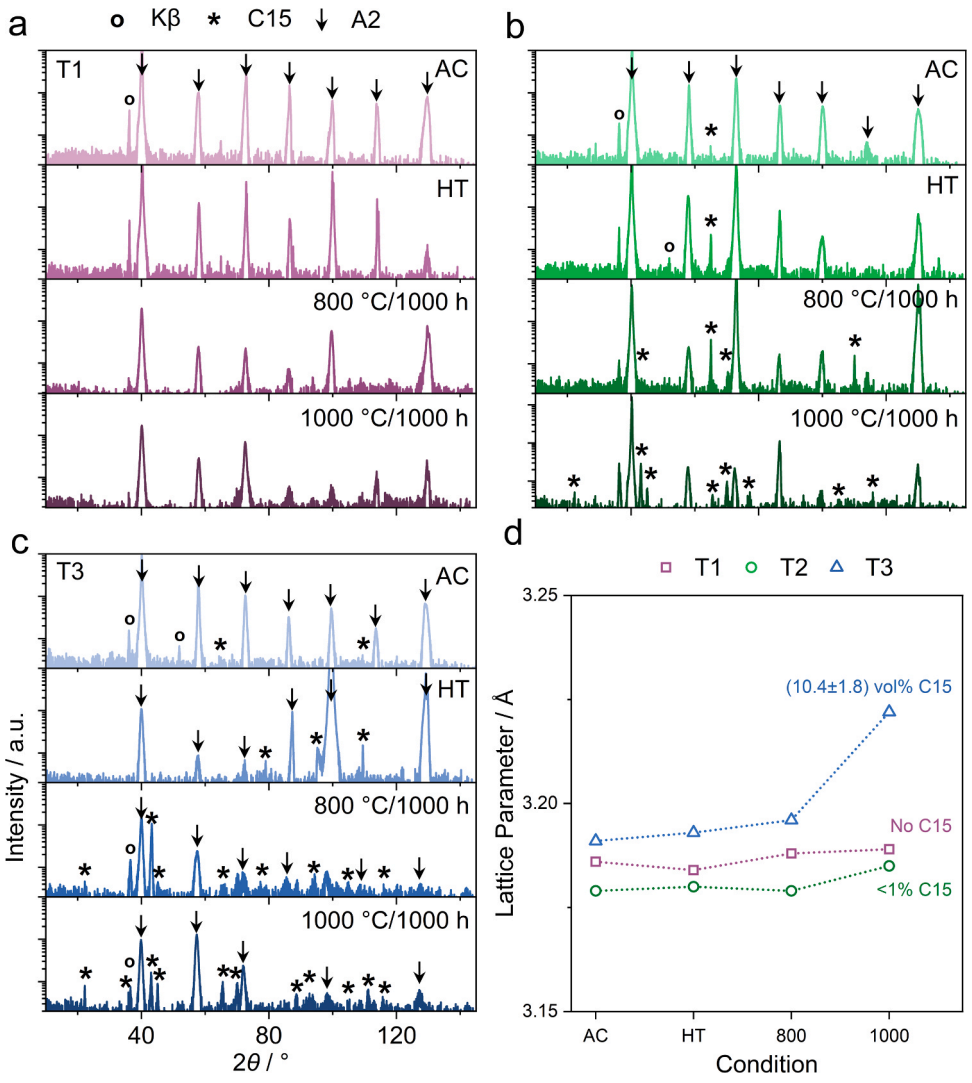

Fig. 3. XRD analysis of AC, HT, 800 °C/1000 h and 1000 °C/1000 h: a) T1 (purple color), b) T2 (green), c) T3 (blue), and d) A2 lattice parameter in the different processing conditions for the three alloys.

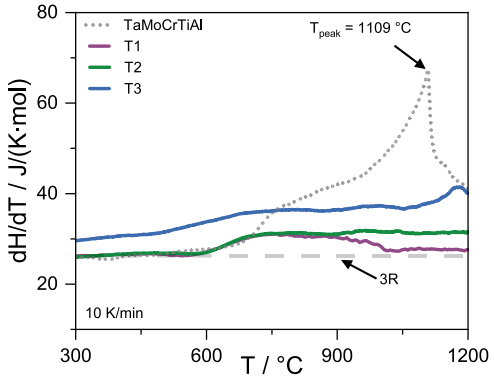

Fig. 4. DSC results (heating with 10 K/min) as derivative of the enthalpy dH/dT. Equimolar TaMoCrTiAl with ordering transformation [34] is included for comparison. The dashed line highlights the thermodynamic limit of $c_p = 3R$.

of (1200 ± 50) MPa. The yield strength gradually decreases to 650–800 MPa in the intermediate temperature range of 400–800 °C, as shown in Fig. 5d. At higher temperatures (900–1000 °C), yield strength further decreases, with T1 and T3 exhibiting more pronounced drops compared to T2. The evolution of yield strength with temperature can be divided into three distinct regions [57–59]:

(i) a regime from RT to 400 °C, where strength decreases due to thermal activation of dislocation motion,
(ii) an athermal regime between 400 and 800 °C, characterized by a plateau in yield strength, where the rate of thermally activated kink-pair nucleation increases,
(iii) a diffusion-controlled regime above 800 °C, where strength degradation is governed by creep deformation.

Further insights into these temperature-dependent regimes are discussed later in this section, specifically in relation to strain hardening behavior.

All alloys exhibit a complex temperature dependence of strain hardening, including slight strain softening at RT, strain hardening at elevated temperatures, and pronounced strain softening at high temperatures. Fig. 6 quantifies these trends by comparing true stress σ_t and true strain hardening $d\sigma_t/d\varepsilon_t$ as a function of true strain ε_t. If no other failure mechanisms occur, the strain at the intersection of the two curves at $d\sigma_t/d\varepsilon_t = \sigma_t$ (Considère criterion) marks the upper limit of strain, the material can achieve through uniform plastic deformation in tension under engineering-relevant loading conditions. The selected temperatures of RT, 600, and 1000 °C cover the three deformation mechanisms

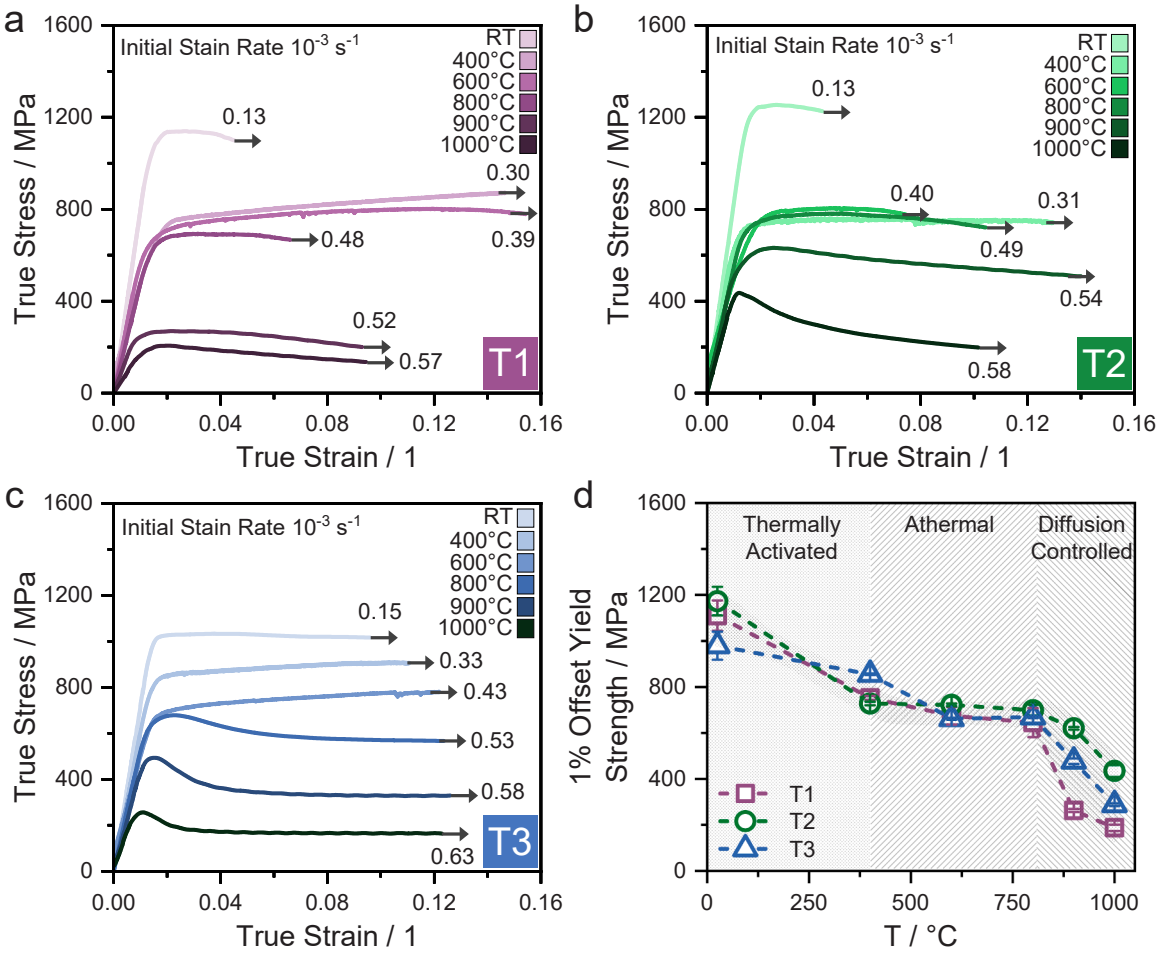

Fig. 5. Mechanical behavior of: a) T1, b) T2, and c) T3, characterized by true compression stress-strain curves. Estimated homologous temperatures (T_S are provided in Supplementary information Table S1) are noted at the stress-strain curves. All tests were deliberately interrupted as indicated by the arrows. d) Compilation of the 1 % offset yield strengths as a function of test temperature.

(a–c) described above.

The true strain at which $d\sigma_t/d\varepsilon_t = \sigma_t$ increases from RT to 600 °C, then decreases again at 1000 °C. This non-monotonic trend reflects the transition between distinct deformation regimes [60]. At RT, the alloys operate in a regime where dislocation motion is assisted by thermal activation of kink-pair formation and propagation [61]. The relatively low strain values at RT suggest early onset of flow instability due to limited strain hardening capacity, if the alloys were tested in tension [62].

At 600 °C, the alloys are in the athermal deformation regime, indicated by a minimal effect of temperature on yield strength. The highest strain hardening capability across all alloys is observed at 400–800 °C. At 1000 °C, diffusion-controlled mechanisms dominate plastic deformation processes [63]. The reduction in true strain at $d\sigma_t/d\varepsilon_t = \sigma_t$ at this temperature reflects a diminished ability to sustain uniform plastic flow [62].

The temperature-dependent behavior discussed above, based on the Considère criterion, highlights the complex interplay between thermal activation, dislocation dynamics, and time-dependent deformation mechanisms in these Ti-rich RCCAs [64].

Fig. 7 shows SEM-BSE micrographs of all three alloys after compression tests. The tests at RT were interrupted at a plastic strain of (4 ± 1) %, while those at elevated temperatures were stopped at (10 ± 1) %. All samples exhibit large grain sizes. At RT (thermally activated region), contrast features are visible in several grains (see, for example, Fig. 7a and c). These features are sharp and straight, indicating slip bands. Furthermore, intersecting slip bands suggest the activation of multiple slip systems in grains of favorable orientation [65].

Fig. 7a-f illustrates post-deformation microstructures for T1–T3 at RT and 600 °C, where intergranular and transgranular cracks are observed. In contrast, at 1000 °C (diffusion-controlled region), intergranular cracking is evident in T1 and T2, while T3 shows no detectable cracking at the same strain level (Fig. 7i). This suggests that T3 may offer improved structural integrity under high-temperature deformation.

The observed strain hardening behavior does not seem to result from dynamic recrystallization, as there is no microstructural evidence supporting its occurrence [66]. Cracks are observed under most conditions, including those showing strain hardening, indicating that stress relaxation through cracking does not consistently cause softening [67]. At 1000 °C, the onset of diffusion-controlled deformation may facilitate dynamic recovery [68], which contributes to the observed strain softening.

Given the large grain sizes, grain rotation is unlikely to contribute significantly to strain softening, but it may play a role in crack formation. Limitations in strain accommodation between differently oriented neighboring grains could lead to grain boundary decohesion, as observed in T1 and T2 (Fig. 7g and h). In contrast, T3—with substantial C15 phase decoration at grain boundaries—exhibits improved boundary integrity (Fig. 7i), suggesting that the Laves phase may help stabilize grain boundaries under high strain. All tests were conducted under compression at a relatively high strain rate. The deformation behavior—particularly the initial stress hump followed by steady-state flow,

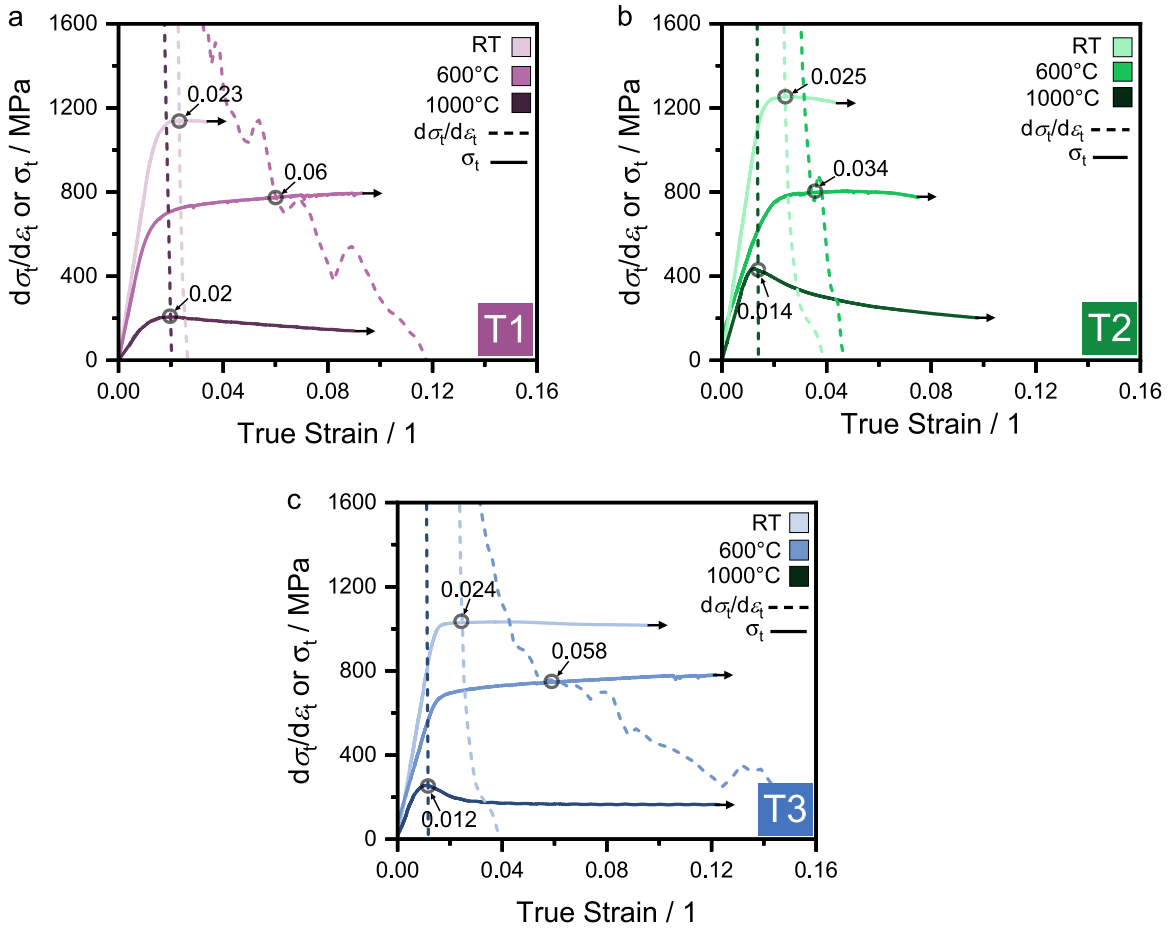

Fig. 6. True stress-strain (σ_t vs. ε_t) and strain hardening $d\sigma_t/d\varepsilon_t$ curves at RT, 600 ℃, and 1000 ℃ of: a) T1, b) T2, and c) T3. The Considère criterion point is illustrated by black circle with corresponding value.

may be influenced by early-stage cracking [69] or strain rate effects [70]. Despite a single-phase or near single-phase microstructures being obtained according to the design goals, strain hardening ability at room temperature remains low and cracks are obtained even under compression loading conditions. Grain refinement by thermomechanical working might reveal the full ductility potential of these alloys. This is not addressed in this screening study.

3.4. Alloy system comparison

In Fig. 8, the yield strengths of T1, T2 and T3 are compared to commercially available Ti-based engineering alloys. As shown in Fig. 8a, the strength of our alloys is comparable to α + β and near-β Ti alloys and exceeds that of α and near-α Ti alloys up to 570 °C [71,72]. Given the differences in density among the compared materials, Fig. 8b presents the density-normalized strength. Although T1 to T3 show slightly lower values than α + β and near-β Ti-alloys, they remain competitive with near-α alloys and show higher strength than single-phase α-Ti alloys up to 570 °C. More importantly, across the 600–1000 °C range — targeted here — T1–T3 demonstrate promising strength retention, even without relying on multi-phase microstructures. This is particularly impressive considering their (nearly) single-phase A2 structure, which typically limits high-temperature strength [73]. Even in the creep-controlled strength regime above 800 °C, these alloys maintain their performance. Notably, T2 achieves a density-normalized strength approximately 50 MPa/(g/cm^3) higher than Ti alloys in the 800–1000 °C range, highlighting the engineering potential of single-phase A2 RCCAs. However, it is important to note that the present data are based on compression tests at a relatively high strain rate, and do not account for creep behavior.

Fig. 9 presents the same assessment using state-of-the-art Ni-based alloys, including superalloys with $\gamma' +$ carbide, $\gamma + \gamma' +$ carbide, $\gamma + \gamma'$, and $\gamma + \gamma' + \gamma''$ microstructures [18]. At temperatures up to 800 °C, T1, T2, and T3 demonstrate competitive or superior yield strength compared to several commercial Ni-based superalloys. Notably, T2 maintains a 0.2 % offset yield strength above 700 MPa at 800 °C, rivaling that of $\gamma + \gamma' +$ carbide-strengthened alloys. However, the complex precipitation-hardened Ni-based alloys generally outperform the single-phase T1, T2, and T3 in absolute strength beyond 900 °C due to precipitation strengthening. In terms of density-normalized strength (Fig. 9b), T1–T3 consistently outperform most Ni-based superalloys across the entire temperature range. This is particularly significant in the RT–900 °C range, where the lower density of T1–T3 results in a clear advantage in density-normalized strength, making them attractive for weight-sensitive aerospace and energy applications.

A focused comparison of single-phase γ Ni-based alloys (Fig. 8b and Fig. 9b) with single-phase T1–T3 reveals that all three alloys significantly outperform their Ni counterparts in both absolute and density-normalized strength up to 900 °C. The single-phase γ alloys, though thermally stable, lack the multiphase strengthening mechanisms of advanced precipitation-strengthened superalloys, resulting in a more pronounced drop in strength at elevated temperatures. Notably, T2 retains over 60 % of its RT strength at 900 °C, underscoring its potential as a lightweight, high-strength alternative to single-phase γ Ni-based alloys in intermediate-temperature applications.

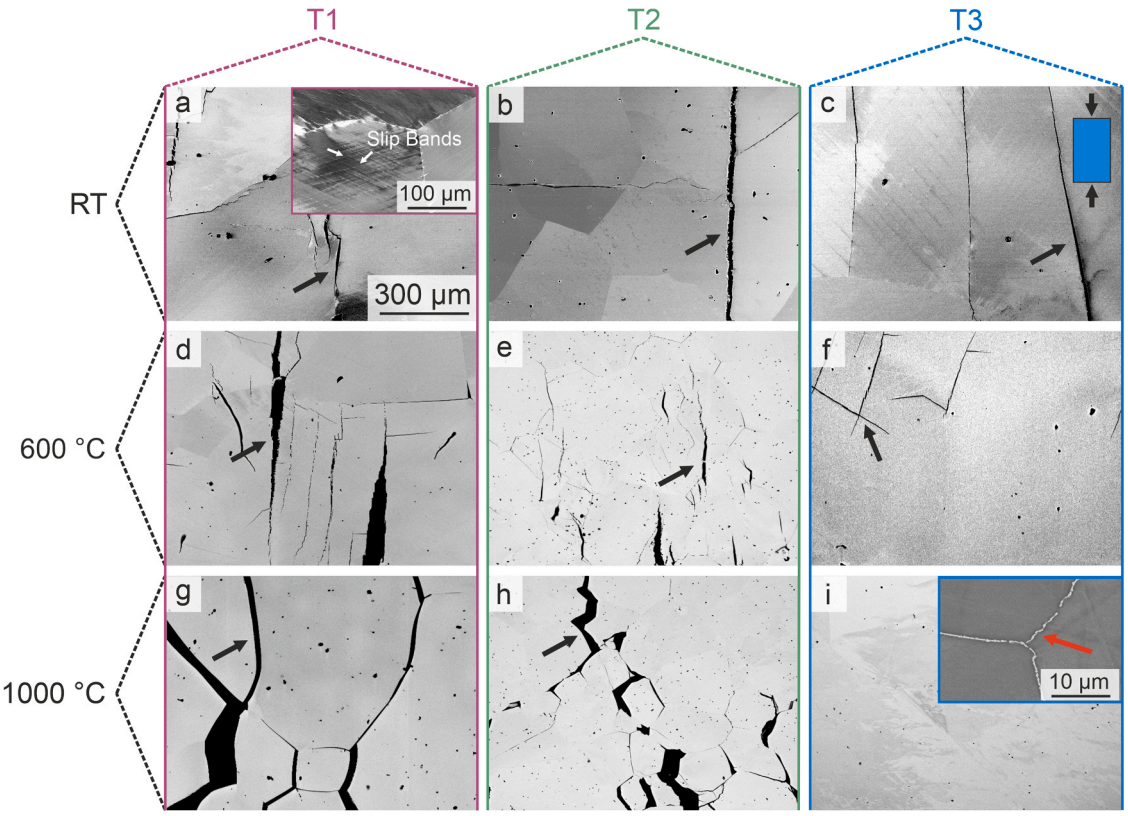

Fig. 7. SEM-BSE micrographs after compression testing of T1 (a,d,g), T2 (b,e,h), and T3 (c,f,j): a–c) RT, d–f) 600 ℃ and g–i) 1000 ℃. The compression direction is vertical as indicated in the inset of (c). White arrows indicate slip bands (inset of a), black arrows indicate cracks, and red arrow indicates Laves phase.

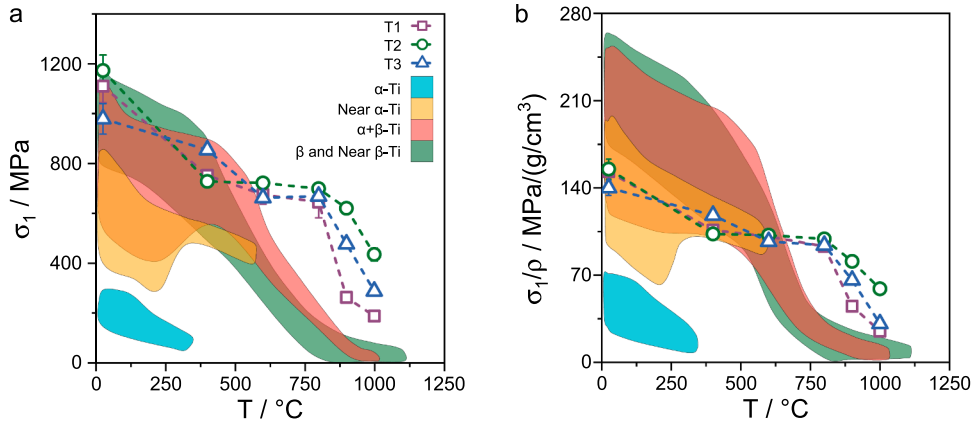

Fig. 8. Comparison of a) temperature-dependent offset yield strength σ_1 of T1–T3 at an initial strain rate of 10^{-3} s^{-1} under compression and b) show the density ρ-normalized offset yield strength with state-of-the-art Ti-based alloys. Note: all reference data are obtained from tensile tests, while the present Ti-rich RCCA data are from compression tests.

4. Conclusions

The current work aims to design lightweight Ti-rich (44–54 at% Ti) alloys in the Ta–Mo–Ti–Cr–Al system suitable for high-temperature applications in the range of 600–1000 °C, to bridge the gap between Ti- and Ni-based alloys. Based on thermodynamic calculations and experimental observations, the following conclusions are drawn:

- All three alloys exhibit the targeted low density of ~ 7.5 g/cm^3, making them suitable for weight-sensitive applications.
- Among the alloys, T1 maintains a stable, single-phase A2 structure from RT up to 1000 °C, even after long-term thermal exposure of up to 1000 h. In contrast, T2 shows low amounts of C15, while T3 exhibits substantial amounts of C15—about 10 %. These differences underscore the role of Mo in stabilizing the A2 matrix. Contrary to thermodynamic calculations, no B2 formation is observed, highlighting the limitations of current thermodynamic models.
- In terms of mechanical properties, T1–T3 exhibit plastic deformability in compression at RT and maintain high strength up to 1000 °C. T2 shows a good combination of thermal stability and mechanical performance, while T3 shows reduced crack formation during mechanical deformation, despite having Laves phase precipitated at the grain boundaries. This is particularly noteworthy as the strain hardening capability remains low in all investigated alloys

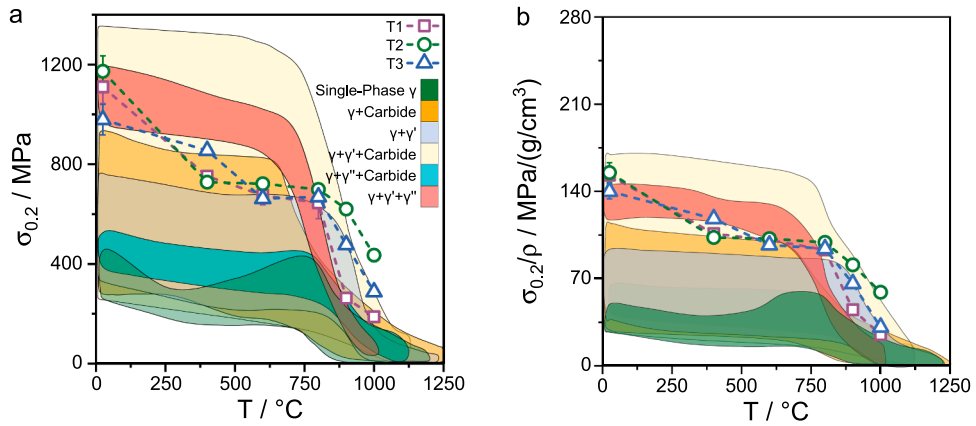

Fig. 9. Comparison of a) temperature-dependent offset yield strength $\sigma_{0.2}$ of T1–T3 at an initial strain rate of 10^{-3} s^{-1} under compression and b) show the density ρ-normalized offset yield strength with state-of-the-art Ni-based alloys. Note: all reference data are obtained from tensile tests, while the present Ti-rich RCCA data are from compression tests.

despite a (near) single-phase microstructure with disordered crystal structure is established.

- Compared to conventional Ti- and Ni-based alloys, these Ti-rich RCCAs demonstrate promising strength retention above 570 °C under compression and show higher strength than single-phase γ Ni-based alloys across the tested temperature range. While these results highlight the potential of Ti-rich RCCAs for intermediate-to-high temperature applications, it should be noted that the current study focuses on high strain rate compression tests. Further investigation into creep behavior is needed to fully assess their suitability for structural applications and to establish these alloys as candidates for bridging the gap between Ti- and Ni-based alloys.

CRediT authorship contribution statement

Martin Heilmaier: Writing – review & editing, Supervision, Resources, Funding acquisition. **Amin Radi:** Writing – review & editing, Writing – original draft, Visualization, Project administration, Methodology, Investigation, Formal analysis, Data curation. **Daniel Schliephake:** Writing – review & editing, Writing – original draft, Investigation, Formal analysis. **Sandipan Sen:** Writing – review & editing, Investigation, Formal analysis. **Chongchong Tang:** Writing – review & editing, Investigation. **R.J. Vikram:** Writing – review & editing. **Jan Lars Riedel:** Writing – review & editing, Investigation. **Liu Yang:** Writing – review & editing. **Shubhashis Dixit:** Writing – review & editing. **Bronislava Gorr:** Writing – review & editing, Supervision, Resources, Funding acquisition. **Alexander Kauffmann:** Writing – review & editing, Writing – original draft, Visualization, Supervision, Methodology, Investigation, Formal analysis, Data curation, Conceptualization.

Declaration of Competing Interest

The authors declare that they have no known competing financial interests or personal relationships that could have appeared to influence the work reported in this paper.

Acknowledgements

We gratefully acknowledge financial support by the Deutsche Forschungsgemeinschaft (DFG) with in the project number of KA 4631/6-1, HE 1872/45-1, KA 4631/4-1, HE 1872/44-1, and GO 2283/8-1. We acknowledge the chemical analysis by HCGE at the Institute for Applied Materials (IAM-AWP) by Dr. Bergfeldt, Karlsruhe Institute of Technology (KIT). We express our gratitude to Dr. Carsten Schroer for his fruitful contribution to this work.

Appendix A. Supporting information

Supplementary data associated with this article can be found in the online version at doi:10.1016/j.jalmes.2025.100219.

Data Availability Statement

The data presented in this study are available in KIT open at https://doi.org/10.35097/rsaezhcaf97uuc1z under CC BY-SA 4.0 license. Further information is available upon request with alexander.kauffmann@rub.de.

References

[1] L.M. Kang, C. Yang, A review on high-strength titanium alloys: microstructure, strengthening, and properties, Adv. Eng. Mater. 21 (2019) 1801359, https://doi.org/10.1002/adem.201801359.
[2] D. Eylon, S. Fujishiro, P.J. Postans, F.H. Froes, High-temperature titanium alloys—a review, JOM 36 (1984) 55–62, https://doi.org/10.1007/BF03338617.
[3] W. Mei, J. Sun, Y. Wen, Martensitic transformation from β to α′ and α″ phases in Ti-V alloys: a first-principles study, J. Mater. Res. 32 (2017) 3183–3190, https://doi.org/10.1557/jmr.2017.276.
[4] R. Sun, G. Mi, Influence of alloying elements content on high temperature properties of Ti-V-Cr and Ti-Al-V series titanium alloys: a JMatPro program calculation study, J. Phys. Conf. Ser. 2639 (2023) 012019, https://doi.org/10.1088/1742-6596/2639/1/012019.
[5] J.D. Beal, R. Boyer, D. Sanders, in: S.L. Semiatin (Ed.), Metalworking: Sheet Forming 14B, ASM International, 2006, https://doi.org/10.31399/asm.hb.v14b.9781627081863.
[6] S. Zhu, C. Zhu, D. Luo, X. Zhang, K. Zhou, Development of a low-density and high-strength titanium alloy, Metals 13 (2023) 251, https://doi.org/10.3390/met13020251.
[7] M. Es-Souni, Creep deformation behavior of three high-temperature near α-Ti alloys: IMI 834, IMI 829, and IMI 685, Metall. Mater. Trans. A 32 (2001) 285–293, https://doi.org/10.1007/s11661-001-0260-1.
[8] J. Dai, J. Zhu, C. Chen, F. Weng, High temperature oxidation behavior and research status of modifications on improving high temperature oxidation resistance of titanium alloys and titanium aluminides: a review, J. Alloy. Compd. 685 (2016) 784–798, https://doi.org/10.1016/j.jallcom.2016.06.212.
[9] F. Hao, J. Xiao, Y. Feng, Y. Wang, J. Ju, Y. Du, K. Wang, L. Xue, Z. Nie, C. Tan, Tensile deformation behavior of a near-titanium alloy Ti-6Al-2Zr-1Mo-1V under a wide temperature range, J. Mater. Res. Technol. 9 (2020) 2818–2831, https://doi.org/10.1016/j.jmrt.2020.01.016.
[10] C.H. Park, B. Lee, S.L. Semiatin, C.S. Lee, Low-temperature superplasticity and coarsening behavior of Ti-6Al-2Sn-4Zr-2Mo-0.1Si, Mater. Sci. Eng.: A 527 (2010) 5203–5211, https://doi.org/10.1016/j.msea.2010.04.082.
[11] L. Mengis, C. Oskay, A. Donchev, M.C. Galetz, Critical assessment of the cyclic oxidation resistance of the aluminized Ti-48Al-2Cr-2Nb TiAl alloy at 700 °C and its impact on mechanical properties, Surf. Coat. Technol. 406 (2021) 126646, https://doi.org/10.1016/j.surfcoat.2020.126646.
[12] R. Pflumm, S. Friedle, M. Schütze, Oxidation protection of γ-TiAl-based alloys – a review, Intermetallics 56 (2015) 1–14, https://doi.org/10.1016/j.intermet.2014.08.002.
[13] O. Genc, R. Unal, Development of gamma titanium aluminide (γ-TiAl) alloys: a review, J. Alloy. Compd. 929 (2022) 167262, https://doi.org/10.1016/j.jallcom.2022.167262.

[14] A. Behera, A.K. Sahoo, S.S. Mahapatra, Application of Ni-based superalloy in aero turbine blade: a review, Proc. Inst. Mech. Eng. Part E: J. Process Mech. Eng. 237 (2023) 1–18, https://doi.org/10.1177/09544089231219104.

[15] Qiu. S., Jiao. Z., Ni-Base Superalloys: Alloying and Microstructural Control, 2022, 133–154. ⟨https://doi.org/10.1007/978-981-19-4743-8_6⟩.

[16] S.K. Selvaraj, G. Sundaramali, S. Jithin Dev, R. Srii Swathish, R. Karthikeyan, K. E. Vijay Vishaal, V. Paramasivam, Recent advancements in the field of Ni-based superalloys, Adv. Mater. Sci. Eng. 2021 (2021) 9723450, https://doi.org/10.1155/2021/9723450.

[17] A.F. Giamei, D.D. Pearson, D.L. Anton, Y/Y: the key to superalloy behavior, MRS online proceedings library 39 (1984) 293–308, https://doi.org/10.1557/PROC-39-293.

[18] Nickel Institute, High-temperature high-strength nickel-base alloys a practical guide to the use of nickel-containing alloys, 393 (2020) 86, ⟨https://nickelinstitute.Org⟩.

[19] Q. Wen, M. Wang, L. Kong, H. Zhu, Effects of alloying elements on the Ni/Ni3Al interface strength and vacancy diffusion behavior, J. Appl. Phys. 128 (2020) 175307, https://doi.org/10.1063/5.0028621.

[20] D. Li, J. Liu, W. Huang, N. Li, K. Liu, Study on mechanical properties of Ni-based superalloys coupled with quantified weights of multi-modal microstructure damage evolution, J. Alloy. Compd. 969 (2023) 172486, https://doi.org/10.1016/j.jallcom.2023.172486.

[21] T.M. Smith, B.D. Esser, N. Antolin, A. Carlsson, R.E.A. Williams, A. Wessman, T. Hanlon, H.L. Fraser, W. Windl, D.W. McComb, M.J. Mills, Phase transformation strengthening of high-temperature superalloys, Nat. Commun. 7 (2016) 13434, https://doi.org/10.1038/ncomms13434.

[22] J. Zhang, F. Lu, L. Li, An overview of thermal exposure on microstructural degradation and mechanical properties in Ni-based single crystal superalloys, Materials 16 (2023) 1787, https://doi.org/10.3390/ma16051787.

[23] S.K. Dewangan, A. Mangish, S. Kumar, A. Sharma, B. Ahn, V. Kumar, A review on High-Temperature applicability: a milestone for high entropy alloys, Eng. Sci. Technol. Int. J. 35 (2022) 101211, https://doi.org/10.1016/j.jestch.2022.101211.

[24] O.N. Senkov, D.B. Miracle, K.J. Chaput, J.P. Couzinie, Development and exploration of refractory high entropy alloys - a review, J. Mater. Res. 33 (2018) 3092–3128, https://doi.org/10.1557/jmr.2018.153.

[25] O.N. Senkov, S.V. Senkova, C. Woodward, D.B. Miracle, Low-density, refractory multi-principal element alloys of the Cr-Nb-Ti-V-Zr system: microstructure and phase analysis, Acta Mater. 61 (2013) 1545–1557, https://doi.org/10.1016/j.actamat.2012.11.032.

[26] O.N. Senkov, S.V. Senkova, D.B. Miracle, C. Woodward, Mechanical properties of low-density, refractory multi-principal element alloys of the Cr–Nb–Ti–V–Zr system, Mater. Sci. Eng.: A 565 (2013) 51–62, https://doi.org/10.1016/j.msea.2012.12.018.

[27] O.N. Senkov, J.M. Scott, S.V. Senkova, F. Meisenkothen, D.B. Miracle, C. F. Woodward, Microstructure and elevated temperature properties of a refractory TaNbHfZrTi alloy, J. Mater. Sci. 47 (2012) 4062–4074.

[28] O.N. Senkov, C.F. Woodward, Microstructure and properties of a refractory NbCrMo0.5Ta0.5TiZr alloy, Mater. Sci. Eng.: A 529 (2011) 311–320, https://doi.org/10.1016/j.msea.2011.09.033.

[29] O.N. Senkov, J.M. Scott, S.V. Senkova, D.B. Miracle, C.F. Woodward, Microstructure and room temperature properties of a high-entropy TaNbHfZrTi alloy, J. Alloy. Compd. 509 (2011) 6043–6048, https://doi.org/10.1016/j.jallcom.2011.02.171.

[30] J. Wang, S. Basu, A. Kauffmann, M. Heilmaier, R. Schwaiger, The effect of grain boundaries and precipitates on the mechanical behavior of the refractory compositionally complex alloy NbMoCrTiAl, Appl. Phys. Lett. 124 (2024) 201905, https://doi.org/10.1063/5.0203536.

[31] S. Laube, G. Winkens, A. Kauffmann, J. Li, C. Kirchlechner, M. Heilmaier, Strength of disordered and ordered Al-containing refractory high-entropy alloys, Adv. Eng. Mater. 26 (2024) 2301797, https://doi.org/10.1002/adem.202301797.

[32] X.B. Feng, J.Y. Zhang, Y.Q. Wang, Z.Q. Hou, K. Wu, G. Liu, J. Sun, Size effects on the mechanical properties of nanocrystalline NbMoTaW refractory high entropy alloy thin films, Int. J. Plast. 95 (2017) 264–277, https://doi.org/10.1016/j.ijplas.2017.04.013.

[33] B. Kang, J. Lee, H.J. Ryu, S.H. Hong, Ultra-high strength WNbMoTaV high-entropy alloys with fine grain structure fabricated by powder metallurgical process, Mater. Sci. Eng.: A 712 (2018) 616–624, https://doi.org/10.1016/j.msea.2017.12.021.

[34] H. Chen, A. Kauffmann, S. Seils, T. Boll, C.H. Liebscher, I. Harding, K.S. Kumar, D. V. Szabó, S. Schlabach, S. Kauffmann-Weiss, F. Müller, B. Gorr, H.J. Christ, M. Heilmaier, Crystallographic ordering in a series of Al-containing refractory high entropy alloys Ta–Nb–Mo–Cr–Ti–Al, Acta Mater. 176 (2019) 123–133, https://doi.org/10.1016/j.actamat.2019.07.001.

[35] S. Laube, S. Schellert, A. Srinivasan Tirunilai, D. Schliephake, B. Gorr, H.J. Christ, A. Kauffmann, M. Heilmaier, Microstructure tailoring of Al-containing compositionally complex alloys by controlling the sequence of precipitation and ordering, Acta Mater. 218 (2021) 117217, https://doi.org/10.1016/j.actamat.2021.117217.

[36] S. Laube, H. Chen, A. Kauffmann, S. Schellert, F. Müller, B. Gorr, J. Müller, B. Butz, H.J. Christ, M. Heilmaier, Controlling crystallographic ordering in Mo–Cr–Ti–Al high entropy alloys to enhance ductility, J. Alloy. Compd. 823 (2020) 153805, https://doi.org/10.1016/j.jallcom.2020.153805.

[37] F. Müller, B. Gorr, H.J. Christ, J. Müller, B. Butz, H. Chen, A. Kauffmann, M. Heilmaier, On the oxidation mechanism of refractory high entropy alloys, Corros. Sci. 159 (2019) 108161, https://doi.org/10.1016/j.corsci.2019.108161.

[38] F. Müller, B. Gorr, H.J. Christ, H. Chen, A. Kauffmann, S. Laube, M. Heilmaier, Formation of complex intermetallic phases in novel refractory high-entropy alloys NbMoCrTiAl and TaMoCrTiAl: thermodynamic assessment and experimental validation, J. Alloy. Compd. 842 (2020) 155726, https://doi.org/10.1016/j.jallcom.2020.155726.

[39] L. Yang, S. Sen, D. Schliephake, R.J. Vikram, S. Laube, A. Pramanik, A. Chauhan, S. Neumeier, M. Heilmaier, A. Kauffmann, Creep behavior of a precipitation-strengthened A2-B2 refractory high entropy alloy, Acta Mater. 288 (2025) 120827, https://doi.org/10.1016/j.actamat.2025.120827.

[40] F. Liang, Y. Sun, H. Wan, Y. Li, W. Lu, A. Meng, L. Gu, Z. Luo, Y. Lin, Y. Zhang, X. Chen, Unlocking wear resistance in an ultrastrong dual-phase high-entropy alloy by interface-constrained deformation of brittle laves phases, Friction 12 (2024) 2389–2398, https://doi.org/10.1007/s40544-024-0884-5.

[41] S. Schellert, B. Gorr, H.J. Christ, C. Pritzel, S. Laube, A. Kauffmann, M. Heilmaier, The effect of al on the formation of a CrTaO4 layer in refractory high entropy alloys Ta-Mo-Cr-Ti-xAl, Oxid. Met. 96 (2021) 333–345, https://doi.org/10.1007/s11085-021-10046-7.

[42] Pandat 2025 Database Manual PanRHEA Database for multi-component refractory high entropy alloys (RHEA), 2025. ⟨https://computherm.com/docs⟩.

[43] J.B. Nelson, D.P. Riley, An experimental investigation of extrapolation methods in the dimensions of crystals derivation of accurate unit-cell, Proc. Phys. Soc. 57 (1945) 160–177.

[44] DIN 51007:2019-04 – thermal analysis – differential scanning calorimetry (DSC) – principles, in: DIN 51007:2019-04, Beuth Verlag GmbH, Berlin, Germany, 2019.

[45] A. Sundar, X. Tan, S. Hu, M.C. Gao, CALPHAD-based Bayesian optimization to accelerate alloy discovery for high-temperature applications, J. Mater. Res. 40 (2025) 112–122, https://doi.org/10.1557/s43578-024-01489-0.

[46] A.E. Mann, J.W. Newkirk, Compositional modifications to alter and suppress laves phases in AlxCrMoTayTi alloys, Adv. Eng. Mater. 25 (2023) 2201614, https://doi.org/10.1002/adem.202201614.

[47] Y. Jiang, S. Zomorodpoosh, I. Roslyakova, L. Zhang, Thermodynamic re-assessment of binary Cr-Nb system down to 0 K, CALPHAD 62 (2018) 109–118, https://doi.org/10.1016/j.calphad.2018.06.001.

[48] A.V. Kazantzis, M. Aindow, I.P. Jones, G.K. Triantafyllidis, J.T.M. De Hosson, The mechanical properties and the deformation microstructures of the C15 laves phase Cr2Nb at high temperatures, Acta Mater. 55 (2007) 1873–1884, https://doi.org/10.1016/j.actamat.2006.10.048.

[49] S. Laube, A. Kauffmann, S. Schellert, S. Seils, A.S. Tirunilai, C. Greiner, Y. M. Eggeler, B. Gorr, H.J. Christ, M. Heilmaier, Formation and thermal stability of two-phase microstructures in Al-containing refractory compositionally complex alloys, Sci. Technol. Adv. Mater. 23 (2022) 692–706, https://doi.org/10.1080/14686996.2022.2132118.

[50] S. Dasari, A. Sharma, V. Soni, Z. Kloenne, H. Fraser, R. Banerjee, Crystallographic and compositional evolution of ordered B2 and disordered BCC phases during isothermal annealing of refractory high-entropy alloys, Microsc. Microanal. 29 (2023) 303–313, https://doi.org/10.1017/S1431927622012053.

[51] H. Chen, Gefüge und Eigenschaften von äquiatomaren Legierungen aus dem System Ta-Nb-Mo-Cr-Ti-Al (Doctoral Thesis), Karlsruhe Institute of Technology, Karlsruhe, 2020, https://doi.org/10.5445/IR/1000118090.

[52] S. Hasan, P. Adhikari, S. San, W.Y. Ching, Phase stability, electronic, mechanical, lattice distortion, and thermal properties of complex refractory-based high entropy alloys TiVCrZrNbMoHfTaW with varying elemental ratios, RSC Adv. 15 (2025) 1878–1895, https://doi.org/10.1039/d4ra07460b.

[53] R.W. Balluffi, L.L. Seigle, Growth of voids in metals during diffusion and creep, Acta Metall. 5 (1957) 449–454, https://doi.org/10.1016/0001-6160(57)90063-9.

[54] R. Kareem, M.R.R. Panicker, V.N.N. Namboothiri, J.S. Bhavan, D. Xavier, P.S. Robi, Synthesis and characterization of novel V30Nb16Ta8Cr30Mo16 refractory high-entropy alloy, J. Mater. Res. (2025), https://doi.org/10.1557/s43578-025-01647-y.

[55] R.J. Vikram, S. Sen, L. Yang, M. Eusterholz, A. Radi, D. Schliephake, J.-P. Couzinié, A. Kauffmann, M. Heilmaier, Ultra-Slow Coarsening in Precipitation-Strengthened Refractory High-Entropy, Alloys 271 (2026) 117026, https://doi.org/10.1016/j.scriptamat.2025.117026.

[56] F. Chu, D.P. Pope, Deformation of C15 laves phase alloys, MRS Online Proc. Libr. 364 (1994) 1197–1208, https://doi.org/10.1557/PROC-364-1197.

[57] Gerd Lütjering, James C. Williams. Titanium, 2nd ed., Springer Berlin, Heidelberg, 2007.

[58] V. Vítek, F. Kroupa, Dislocation theory of slip geometry and temperature dependence of flow stress in B.C.C. metals, Phys. Status Solidi (b) 18 (1966) 703–713, https://doi.org/10.1002/pssb.19660180222.

[59] G. Taylor, Thermally-activated deformation of BCC metals and alloys, Prog. Mater. Sci. 36 (1992) 29–61, https://doi.org/10.1016/0079-6425(92)90004-Q.

[60] N. Zotov, B. Grabowski, Entropy of kink pair formation on screw dislocations: an accelerated molecular dynamics study, Model Simul. Mater. Sci. Eng. 30 (2022) 065004, https://doi.org/10.1088/1361-651X/ac7ac9.

[61] P. Garg, K. Hemker, I.J. Beyerlein, Stress and temperature dependence of screw dislocation motion in refractory multi-principal element alloys, High Entropy Alloys Mater. (2025) 1–17, https://doi.org/10.1007/s44210-025-00062-6.

[62] R.R. Eleti, M. Klimova, M. Tikhonovsky, N. Stepanov, S. Zherebtsov, Exceptionally high strain-hardening and ductility due to transformation induced plasticity effect in Ti-rich high-entropy alloys, Sci. Rep. 10 (1) (2020) 13293, https://doi.org/10.1038/s41598-020-70298-2.

[63] X. Wu, R. Liu, F. Khelfaoui, Creep phenomena, mechanisms, and modeling of complex engineering alloys, Modelling 5 (2024) 819–840, https://doi.org/10.3139/ijmr-2002-0130.

[64] W.C. Emmens, Appendix: the Considère condition, in: W.C. Emmens (Ed.), Formability: A Review of Parameters and Processes that Control, Limit or Enhance

the Formability of Sheet Metal, Springer Berlin Heidelberg, Berlin, Heidelberg, 2011, pp. 97–101, https://doi.org/10.1007/978-3-642-21904-7_19.
[65] D. Caillard, B. Bienvenu, E. Clouet, Anomalous slip in body-centred cubic metals, Nature 609 (2022) 936–941, https://doi.org/10.1038/s41586-022-05087-0.
[66] F. Montheillet, D. Piot, N. Matougui, M.L. Fares, A critical assessment of three usual equations for strain hardening and dynamic recovery, Met. Mater. Trans. A Phys. Met. Mater. Sci. 45 (2014) 4324–4332, https://doi.org/10.1007/s11661-014-2388-9.
[67] K. Srivastava, D. Weygand, D. Caillard, P. Gumbsch, Repulsion leads to coupled dislocation motion and extended work hardening in bcc metals, Nat. Commun. 11 (1) (2020) 5098, https://doi.org/10.1038/s41467-020-18774-1.
[68] D. Sun, M. Li, Y. Zou, R. Yang, F. Li, A model for dynamic recovery of bcc structure, Chin. Sci. Bull. 42 (1997) 1211–1215, https://doi.org/10.1007/BF02882851.
[69] D. Wei, Z. Jiang, J. Han, Evolution of internal crack in BCC Fe under compressive loading, J. Mod. Phys. 03 (2012) 1594–1601, https://doi.org/10.4236/jmp.2012.310197.
[70] E. El-Magd, Mechanical properties at high strain rates, J. de Phys. IV Fr. 4 (1994) 149–170, https://doi.org/10.1051/jp4:1994823.
[71] D. Eylon, S. Fujishiro, F.H. Froes, Titanium alloys for high temperature applications — a review, High Temp. Mater. Process. 6 (1984) 81–92, https://doi.org/10.1515/HTMP.1984.6.1-2.81.
[72] R. Canumalla, T.V. Jayaraman, Decision science driven selection of high-temperature conventional Ti alloys for aeroengines, Aerospace 10 (2023) 211, https://doi.org/10.3390/aerospace10030211.
[73] V. Anil Kumar, R.K. Gupta, M.J.N.V. Prasad, S.V.S. Narayana Murty, Recent advances in processing of titanium alloys and titanium aluminides for space applications: a review, J. Mater. Res. 36 (2021) 689–716, https://doi.org/10.1557/s43578-021-00104-w.